# Adaptive Image-Based Moving-Target Tracking Control of Wheeled Mobile Robots With Visibility Maintenance and Obstacle Avoidance

Shi-Lu Dai<sup>®</sup>, Member, IEEE, Jianjun Liang<sup>®</sup>, Ke Lu<sup>®</sup>, and Xu Jin<sup>®</sup>, Member, IEEE

Abstract—This article presents an adaptive image-based visual servoing (IBVS) for nonholonomic wheeled mobile robots to solve the moving-target tracking problem in obstacle environments. A pinhole camera that is equipped with the following robot to monitor the target' motion is limited field of view (FOV), which relates to the issue of visibility maintenance. Safety navigation is another concern, which requires that the following robot can avoid collisions with the target and static obstacles. Under the IBVS framework, we design novel constrained boundary functions based on pixel coordinate, which can be deviated away from zero to ensure that the following robot drives away from obstacles because obstacle avoidance is a higher priority rather than the tracking task. When there is no obstacle detected, the constrained boundary functions are taken as exponentially decaying functions of time. Using fixed-time stability and control Lyapunov synthesis, the tracking errors are shown to converge in fixed time to a small neighborhood of the desired obstacle-avoidance trajectory generated from the centerline of constrained boundaries while guaranteeing visibility maintenance and obstacle/collision avoidance. The proposed fixed-time IBVS controller (FTIBVSC) only depends on locally relative information acquired by onboard sensors without the need of knowing the feature height and target's velocity. Simulation and experiment studies are carried out to show the efficacy of the proposed FTIBVSC.

Manuscript received 19 May 2023; revised 6 September 2023; accepted 8 October 2023. Date of publication 21 November 2023; date of current version 26 February 2024. The work of Shi-Lu Dai and Ke Lu was supported in part by the National Natural Science Foundation of China under Grant 61973129, Grant 42227901, Grant 62273156, and Grant 62073090; in part by the Guangdong Basic and Applied Basic Research Foundation under Grant 2021A1515012004 and Grant 2023A1515011423; and in part by the Innovation Group Project of Southern Marine Science and Engineering Guangdong Laboratory (Zhuhai) under Grant SML2022008. The work of Xu Jin was supported in part by the United States National Science Foundation under Grant 2131802. Recommended by Associate Editor C. Yang. (Corresponding author: Xu Jin.)

Shi-Lu Dai is with the School of Automation Science and Engineering, Key Laboratory of Autonomous Systems and Networked Control of Ministry of Education, South China University of Technology, Guangzhou 510641, China, and also with the Southern Marine Science and Engineering Guangdong Laboratory (Zhuhai), Zhuhai 519000, China (e-mail: audaisl@scut.edu.cn).

Jianjun Liang was with the School of Automation Science and Engineering, South China University of Technology, Guangzhou 510641, China. He is now with Shenzhen Dajiang Innovation Technology Company Ltd., Shenzhen 518057, China (e-mail: olieliang@163.com).

Ke Lu is with the School of Automation Science and Engineering, South China University of Technology, Guangzhou 510641, China (e-mail: lukenanlin@163.com).

Xu Jin is with the Department of Mechanical and Aerospace Engineering, University of Kentucky, Lexington, KY 40506 USA (e-mail: xu.jin@uky.edu). Digital Object Identifier 10.1109/TCST.2023.3331553

Index Terms—Fixed-time control, image-based visual servoing (IBVS), moving-target tracking, obstacle avoidance, visibility maintenance.

```
Nomenclature
R_i
             Wheeled mobile robot R_i, i \in \{l, f\}.
\mathcal{F}_0
             Earth-fixed frame.
             Body-fixed frame of robot R_i, i \in \{l, f\}.
             Body-fixed frame of the camera.
             Obstacle O_j, j \in \mathcal{N} = \{1, 2, \dots, N\}.
P_{ci}
             Center point of robot R_i, i \in \{l, f\}.
             Closest point on Line 0 to the edge of obstacle
             Position of the center point P_{ci} of robot R_i
(x_i, y_i)
             Heading angle (orientation) of robot R_i in \mathcal{F}_0.
\theta_{lf}
             Relative orientation between robot R_l and
             robot R_f.
             Linear velocity control input of the robot R_i.
v_i
             Angular velocity control input of the robot R_i.
\omega_i
             Radius of the circular safe zone of robot R_i.
d_{lf}
             Distance between P_{cl} and P_{cf}.
             Minimum distance between P_{ci} and the edge
r_{j,i}
             Minimum distance between P_{Oi} and the edge
d_i
\lambda_i
             Line parameter of P_{Oi} on Line 0.
             Overlap distance between robot R_f and the
\rho_j
             obstacle O_i.
             Height between the optical center of the
             camera and P_{cf}.
             Feature height, which is an unknown height
             between the feature point and the optical center
             x-coordinate of the feature point in \mathcal{F}_f.
x_{p,f}
             y-coordinate of the feature point in \mathcal{F}_f.
y_{p,f}
             z-coordinate of the feature point in \mathcal{F}_f.
z_{p,f}
             x-coordinate of the feature point in \mathcal{F}_c.
x_{p,c}
             y-coordinate of the feature point in \mathcal{F}_c.
y_{p,c}
             z-coordinate of the feature point in \mathcal{F}_c.
z_{p,c}
             Pixel coordinate of the feature point on the
(m, n)
             image plane.
             Pixel coordinate of the principal point on the
(m_0, n_0)
```

1063-6536 © 2023 IEEE. Personal use is permitted, but republication/redistribution requires IEEE permission. See https://www.ieee.org/publications/rights/index.html for more information.

image plane.

 $\begin{array}{lll} (m_d,n_d) & \text{Desired pixel coordinate of feature point.} \\ A & \text{Intrinsic matrix of the camera.} \\ a_m,\ a_n & \text{Scaling constants along the $x$-axis and $y$-axis of $\mathcal{F}_c$.} \\ e_m,\ e_n & \text{Tracking errors.} \\ \beta_* & \text{Constrained boundary functions,} \\ & * \in \{mL,mH,nL,nH\}. \\ \\ \mu_* & \text{Time derivatives of the constrained boundary functions $\beta_*$.} \\ \eta_m,\ \eta_n & \text{Error transformations of $e_m$ and $e_n$.} \end{array}$ 

## I. INTRODUCTION

 $f_1, f_2, f_{12}$ 

Activation functions for obstacle avoidance.

7 ISION-BASED control, also known as visual servoing [1], has recently received an increasing attention in robotics since it simply employs the visual information of a camera as feedback signals to determine robot motion. Compared with traditional sensors, e.g., radar and light detection and ranging (LiDAR), cameras have been strongly tied to robotic applications due to their low prices and the rich information they provide. Visual servoing can be classified into two basic categories: position-based visual servoing (PBVS) [2], [3] and image-based visual servoing (IBVS) [4], [5], [6]. In PBVS control design, the controllers are developed based on the relative pose of the target recovered by visual feedback information. PBVS typically requires either geometric knowledge or depth information of the target to be known. To eliminate the need for depth information, several elegant control design techniques [7], [8] were proposed for pose regulation tasks with simultaneous depth identification. Even though the dependence on depth information is reduced in PBVS control design, the control performance may significantly deteriorate when the camera is not perfectly calibrated or the geometric/depth information of the target is inaccurate. In contrast, IBVS employs the pixel coordinate of a feature point as feedback information and thus has robustness against camera calibration errors without the need for geometric/depth information.

One of the most significant problems concerning visionbased moving-target tracking control is the visibility to the target since the visual feedback information is essential to the implementation of controllers. The loss of visibility may happen when either the target is outside the limited field of view (FOV) of the camera or the target is occluded by obstacles in the workspace. Hence, visibility maintenance with the target should be considered in moving-target control design. Consequently, many vision-based tracking control strategies have been proposed to enforce the FOV constraints in controller design [9], [10], [11], [12]. In [9] and [10], a path planning technique was presented to online generate an occlusion-free reference path, and then, vision-based controllers were designed to guarantee that autonomous vehicles track the optimized path without the violation of FOV constraints. In [11], the design of adaptive reference trajectories that satisfy the FOV constraints was developed to address the enclosing and tracking problem of a group of unicycle-type mobile robots. How to develop an IBVS control design without the need of the online reference trajectory generation while handling FOV constraints and vehicle/obstacle occlusion is a challenging research topic that has not yet been fully addressed in the literature.

In addition to visibility maintenance, another critical safety problem is collision/obstacle avoidance, which requires that the following robot does not collide with the moving target or/and obstacles. The artificial potential field is typically employed to deal with the problem of collision/obstacle avoidance [13], [14], [15]. In [13], a formation tracking controller was designed to tackle the spatial constraints induced by obstacles and the borders of the workspace based on an artificial potential field. Nevertheless, when multiple objectives/ constraints need to be considered simultaneously, for instance, moving-target tracking, visibility maintenance, and collision avoidance, designing a potential function for these multiple tasks may increase the risk of converging into local minima. Instead of the design of potential functions, barrier Lyapunov functions (BLFs) have been incorporated into controller design for various types of constraints, e.g., recently presented in [16], [17], [18], and [19], where the constraint requirements from visibility maintenance and collision avoidance were addressed simultaneously. An IBVS for leader-follower formation of mobile robots was presented in [18], where the FOV constraints with guaranteed transient and steady-state performances were solved, but the collision avoidance between the leader and followers was not fully considered. Furthermore, none of these BLF control designs has considered obstacle avoidance. In the typical BLF control designs, e.g., [18], [19], the constraints require that tracking errors are always within a neighborhood of the origin. When obstacle avoidance is considered, tracking errors along with time-varying constraints are expected to deviate from the origin due to the higher priority of obstacle avoidance. In [20], novel switching functions were introduced to modify the nominally exponential behavior of performance functions [21] such that tracking errors deviated from the origin in order to achieve the safety specifications of collision and obstacle avoidance as well as connectivity maintenance.

The convergence speed is an important performance indicator for a control system. In many practical applications, it is desired to achieve tracking control in a finite/fixed time. A practical fixed-time consensus framework for integrator-type multiagent systems was developed in [22] to reduce the magnitude of the initial control input. In [23], adaptive fixed-time control was proposed for output tracking problems of a class of nonlinear systems with asymmetric output constraint requirements, in which tracking error can converge into a small neighborhood of zero with a fixed-time convergence rate. How to develop an IBVS control design technique for solving the moving-target tracking problem, such that tracking error can converge in fixed time to a small residual set without violation of constraint requirements, is also one of the main motivations for this work.

This work addresses the image-based moving-target tracking control problem of nonholonomic wheeled mobile robots, where visibility maintenance, collision/obstacle avoidance, and prescribed performance are integrated in a unified BLF control design framework. To cope with the issues of limited visual

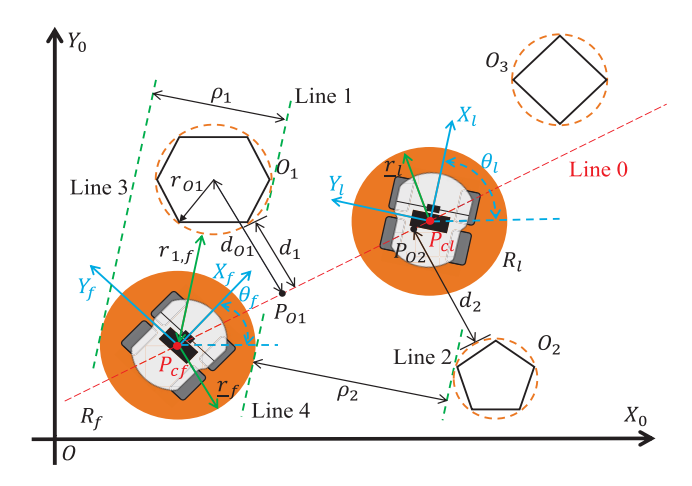


Fig. 1. Schematics of two robots operating in an obstacle environment. Line 0 (red dashed line) is the connecting line between two points  $P_{cl}$  and  $P_{cf}$ . Lines 1-4 (green dashed lines) contact with obstacles  $O_1$ ,  $O_2$ , and the circular safe zone of  $R_f$ , and they are parallel to the heading direction of  $R_l$ .

capability and safe navigation, FOV and time-varying boundary constraints are imposed to ensure that the following robot never breaks the visibility connection and never collides with the target and static obstacles during the whole operation. The constrained boundary functions based on pixel coordinate need to be carefully constructed, which behave differently in the presence of different obstacles. To satisfy the time-varying boundary constraints, BLFs are incorporated into the IBVS control design. The technical contributions of this work are summarized as follows.

- 1) We construct novel constrained boundary functions in a pixel coordinate system, which can be deviated away from zero to ensure that the following robot drives away from obstacles because obstacle avoidance is a higher priority rather than the tracking task. When there is no obstacle detected, the constrained boundary functions are taken as exponentially decaying functions of time, also known as performance functions [21], [24], which can describe predefined transient and steady-state performances of the tracking errors.
- 2) In addition to obstacle avoidance, collision avoidance and visibility maintenance with the target are guaranteed during the whole operation without the need of knowing the feature height and target's velocity even though the obstacles present.
- 3) Compared with the recent IBVS results [18], [19], the proposed IBVS controller not only guarantees prescribed transient and steady-state performances but also achieves fixed-time convergence of tracking errors to a small neighborhood of a desired obstacle-avoidance trajectory.

## II. PROBLEM FORMULATION AND PRELIMINARIES

### A. Robot Model

Two nonholonomic wheeled mobile robots moving on a plane cluttered with static obstacles are shown in Fig. 1. For the motion description of the wheeled mobile robots, the system variables and parameters are defined in the Nomenclature. The leading robot  $R_l$  denotes the moving target to be tracked by robot  $R_f$ . The kinematic models of robots  $R_i$ ,  $i \in \{l, f\}$ , are described by

$$\dot{x}_i = v_i \cos \theta_i \tag{1}$$

$$\dot{y}_i = v_i \sin \theta_i \tag{2}$$

$$\dot{y}_i = v_i \sin \theta_i \tag{2}$$

$$\dot{\theta}_i = \omega_i. \tag{3}$$

Assume that every robot  $R_i$  has a circular safe zone (denoted by the orange circle in Fig. 1) that centers at  $P_{ci}$  with a radius of  $\underline{r}_i$ . If the relative distance  $d_{lf}$  satisfies the following inequality:

$$d_{lf} = \sqrt{\left(x_l - x_f\right)^2 + \left(y_l - y_f\right)^2} \ge \underline{r}_l + \underline{r}_f \tag{4}$$

then there is no collision between robots  $R_l$  and  $R_f$ .

#### B. Obstacle Model

In this work, we address the vision-based target tracking problem in an obstacle environment. More specifically, our objective is to design an IBVS controller such that robot  $R_f$ follows the moving target  $R_l$  while guaranteeing collision/ obstacle avoidance. Let  $\mathcal{N} = \{1, 2, \dots, N\}$  denote the index set of the static obstacle  $O_j$ ,  $j \in \mathcal{N}$ . Assume that the static obstacle  $O_i$  has a virtually circular zone covered by a geometrical radius  $r_{Oj}$ . The position of the obstacle  $O_j$ relative to the robot  $R_f$  can be extracted by an onboard radar or LiDAR. As shown in Fig. 1, for example, two mobile robots  $R_l$  and  $R_f$  are operating in an obstacle environment with N = 3 static obstacles. Line 0 (denoted by the red dashed line in Fig. 1) is the line that connects  $P_{cl}$  and  $P_{cf}$ , and thus, the coordinate (x, y) of a point on Line 0 in the Earth-fixed frame  $\mathcal{F}_0$  can be formulated as

$$\begin{bmatrix} x \\ y \end{bmatrix} = \lambda \begin{bmatrix} x_f \\ y_f \end{bmatrix} + (1 - \lambda) \begin{bmatrix} x_l \\ y_l \end{bmatrix}$$

where  $\lambda$  is known as a line parameter. The value of  $\lambda_i$ indicates the position of  $P_{Oj}$  on Line 0. More specifically,  $P_{Oj}$  is ahead of  $R_l$  if  $\lambda_j < 0$ ,  $P_{Oj}$  is behind  $R_f$  if  $\lambda_j > 1$ , and  $P_{O_i}$  lies between  $R_l$  and  $R_f$  if  $0 < \lambda_i < 1$ .

When there are multiple obstacles in the tracking control system, it is reasonable to only consider the most dangerous or the nearest obstacle at a time. In this work, we consider both the nearest obstacle on the left of Line 0 and the one on the right. For  $0 < \lambda_i < 1$ , the obstacle  $O_i$  is considered as the most dangerous one on the left/right, if it has the minimum distance  $d_i$  among all alternative obstacles on the same side of Line 0. The minimum distance  $d_i$  can be computed by the geometrical relation, e.g.,  $d_j = d_{Oj} - r_{Oj}$ , where the center of circle that covers the obstacle  $O_j$  is measured by an onboard radar or LiDAR such that the distance  $d_{Oi}$  and the radius  $r_{Oi}$ are obtained. For instance, in Fig. 1, the obstacle  $O_1$  is the most dangerous obstacle on the left because  $0 < \lambda_1 < 1$  and  $\lambda_3 < 0$ , and the obstacle  $O_2$  is the most dangerous obstacle on the right. To simplify the notation, we specify  $O_1$  and  $O_2$  as the most dangerous obstacle on the left and the one on the right under any circumstance. Hence, we only need to consider the most dangerous obstacle index  $j \in \{1, 2\}$  hereafter. Note that there is no occlusion caused by the obstacles as long as

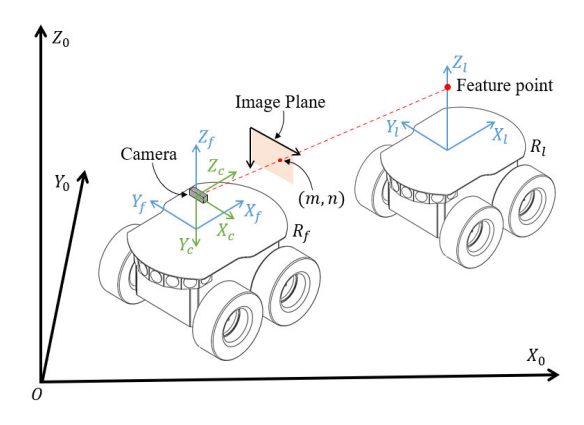


Fig. 2. Camera setup for the visual servoing system.

 $d_1 > 0$  and  $d_2 > 0$ . Robots  $R_i$ ,  $i \in \{l, f\}$ , are collision-free with obstacles if and only if  $r_{j,i} > \underline{r}_i$ , j = 1, 2.

Lines 1–4 denoted by the green dashed lines shown in Fig. 1 contact with the nearest obstacles  $O_1$ ,  $O_2$ , and the circular safe zone of  $R_f$ , and they are parallel to the heading direction of  $R_l$ . More specifically, Lines 1 and 4 shown in Fig. 1 are on the right side of the obstacle  $O_1$  and the robot  $R_f$ , respectively, and Lines 2 and 3 are on the left side of  $O_2$  and  $R_f$ , respectively, when we are facing the heading direction of the target  $R_l$ . These lines in the Earth-fixed frame  $\mathcal{F}_0$  can be described by  $\sin(\theta_l)x - \cos(\theta_l)y + C_k = 0, k = 1, 2, 3, 4$ , where (x, y) denotes the coordinate of a point on a line and  $|C_k|$ represents the distance from the origin to Line k. As shown in Fig. 1,  $\rho_1$  and  $\rho_2$  are called the overlap distances, which can be computed by  $\rho_1 = C_3 - C_1$  and  $\rho_2 = C_2 - C_4$ , respectively. It is clear that  $|\rho_1|$  and  $|\rho_2|$  are the distances between Lines 1 and 3, and between Lines 2 and 4, respectively. If Line 1 is on the right side of Line 3, then the obstacle  $O_1$  overlaps with the circular safe zone of the robot  $R_f$  and  $\rho_1 \ge 0$ . Otherwise, there is no overlap and  $\rho_1 < 0$ . Similar properties hold for the distance  $\rho_2$  between Lines 2 and 4.

#### C. Pinhole Camera Model

As shown in Fig. 2, a monocular pinhole camera is equipped with the following robot  $R_f$  to obtain visual information of the target  $R_l$ . The origin of the camera frame  $\mathcal{F}_c$  is coincident with the optical center of the camera. We assume that the camera's optical center lies on the z-axis of the robot's body-fixed frame  $\mathcal{F}_f$ , that is, the coordinate of the optical center in  $\mathcal{F}_f$  is  $(0,0,h_c)$ , and its optical axis is aligned with the heading direction of robot  $R_f$ . Moreover, there is a feature point on the z-axis of the target frame  $\mathcal{F}_l$ , whose pixel coordinate on the image plane is employed to calculate the tracking errors. Then, the feature point's coordinate in the robot's body-fixed frame  $\mathcal{F}_f$  can be described by

$$\begin{bmatrix} x_{p,f} \\ y_{p,f} \\ z_{p,f} \end{bmatrix} = \begin{bmatrix} \cos \theta_f & \sin \theta_f & 0 \\ -\sin \theta_f & \cos \theta_f & 0 \\ 0 & 0 & 1 \end{bmatrix} \begin{bmatrix} x_l - x_f \\ y_l - y_f \\ h + h_c \end{bmatrix}$$
(5)

where  $[x_{p,f}, y_{p,f}, z_{p,f}]^T$  is the feature point's coordinate in  $\mathcal{F}_f$  and  $h \neq 0$  is the unknown feature height between the optical center of the camera and the feature point. According

to the imaging principle of the pinhole camera, the pixel coordinate (m, n) of the feature point on the image plane is given by

$$\begin{bmatrix} m \\ n \\ 1 \end{bmatrix} = \frac{1}{z_{p,c}} AP \tag{6}$$

with

$$A = \begin{bmatrix} a_m & 0 & m_0 \\ 0 & a_n & n_0 \\ 0 & 0 & 1 \end{bmatrix}; \quad P = \begin{bmatrix} x_{p,c} \\ y_{p,c} \\ z_{p,c} \end{bmatrix}$$

where A is known as the intrinsic matrix of the camera and P denotes the coordinate of the feature point in the camera frame  $\mathcal{F}_c$ . Note that the feature height h is an unknown constant, and its sign is coincident with the sign of  $(n_0 - n)$ , which can be easily determined by the feedback information. Without loss of generality, we assume that h > 0.

Using the relationship between the frames  $\mathcal{F}_c$  and  $\mathcal{F}_f$  shown in Fig. 2, we can rewrite (6) as

$$\begin{bmatrix} m \\ n \end{bmatrix} = \frac{1}{x_{p,f}} \begin{bmatrix} \vec{a}_1 \\ \vec{a}_2 \end{bmatrix} \begin{bmatrix} -y_{p,f} \\ -h \\ x_{p,f} \end{bmatrix}$$
 (7)

where  $\vec{a}_1$  and  $\vec{a}_2$  are the first row and second row of the intrinsic matrix A, respectively. Differentiating (7) along systems (1)–(3) and (5) obtains

$$\begin{bmatrix} \dot{m} \\ \dot{n} \end{bmatrix} = \begin{bmatrix} \frac{q}{h} (m_0 - m) & a_m + (m - m_0) p \\ \frac{q}{h} (n_0 - n) & (n - n_0) p \end{bmatrix} \begin{bmatrix} v_f \\ \omega_f \end{bmatrix} + \frac{q v_l}{h} \begin{bmatrix} a_m \sin \theta_{lf} + (m - m_0) \cos \theta_{lf} \\ (n - n_0) \cos \theta_{lf} \end{bmatrix}$$
(8)

with  $p = -y_{p,f}/x_{p,f} = (m - m_0)/a_m$  and  $q = -h/x_{p,f} = (n - n_0)/a_n$ , where  $\theta_{lf} = \theta_l - \theta_f$  is the relative orientation, and the linear velocity  $v_f$  and the angular velocity  $w_f$  are taken as the control inputs to be designed.

#### D. Modeling of the Visibility Constraints

Because of the limited FOV of the camera, the pixel coordinate (m, n) is subject to the following constraints:

$$m_{\min} \le m \le m_{\max}, \quad n_{\min} \le n \le n_{\max}$$
 (9)

where  $m_{\min}$ ,  $m_{\max}$ ,  $n_{\min}$ , and  $n_{\max}$  are constant parameters that are determined by the pixel resolution of the camera. Violating the FOV constrain (9) implies that the feature point is no longer visible to robot  $R_f$ , that is, the visibility connectivity between  $R_l$  and  $R_f$  is broken.

In addition to the FOV constraint, the inequality (4) can be modeled with pixel coordinate as well. From (6), we know that n is a function of  $y_{p,c}$  and  $z_{p,c}$ . Since the robots are moving on a plane, which means that  $y_{p,c} = -h$ , it follows from (6) that:

$$n = -a_n \frac{h}{z_{p,c}} + n_0.$$

Furthermore, the relative distance  $d_{lf}$  between the moving target  $R_l$  and the follower  $R_f$  can be represented by the

feature point coordinate in  $\mathcal{F}_c$ , i.e.,  $d_{lf} = (x_{p,c}^2 + z_{p,c}^2)^{1/2}$ . According to (4), a sufficient condition for collision avoidance between  $R_l$  and  $R_f$  is  $z_{p,c} \geq \underline{r}_l + \underline{r}_f$ , which requires  $n \geq -a_n h/(\underline{r}_l + \underline{r}_f) + n_0$ . Accordingly, constraint (9) can be rewritten as

$$m_{\min} \le m \le m_{\max}, \quad \underline{n} \le n \le n_{\max}$$
 (10)

where  $\underline{n} \ge \max\{n_{\min}, -a_n h/(\underline{r}_l + \underline{r}_f) + n_0\}$ . It should be noted that inequality (10) is obtained under the assumption h > 0. If h < 0, the constraint imposed on n becomes  $n_{\min} \le n \le \overline{n}$ , where  $\overline{n} \le \min\{n_{\max}, -a_n h/(\underline{r}_l + \underline{r}_f) + n_0\}$ . Define the tracking errors of pixel coordinate as

where  $(m_d, n_d)$  is the desired pixel coordinate of the feature point. Substituting (11) into (10) yields

$$m_{\min} - m_d \le e_m \le m_{\max} - m_d \tag{12}$$

$$n - n_d \le e_n \le n_{\text{max}} - n_d. \tag{13}$$

If constraints (12) and (13) are not violated, then inequality (10) holds, which implies that the FOV constraint (9) and no collision between the robots are guaranteed simultaneously.

## E. Control Objective

We assume that the moving target (leading robot)  $R_l$  is controlled by human operators or intelligent decision-making programs [25]. Hence, we do not consider control design for the moving target  $R_l$  and only design an IBVS controller for the follower  $R_f$ . Accordingly, we make the following assumptions and formulate the control objective.

Assumption 1: The target  $R_l$  moves along a collision-free and feasible trajectory during the whole operation. Moreover, between two obstacles that the moving target  $R_l$  passes through, there is enough space for  $R_f$  to pass through.

Assumption 2: There is no communication between the robots. The follower  $R_f$  has no knowledge about  $v_l$  and  $\omega_l$  and vice versa. The linear velocity of robot  $R_l$  and its time derivative are bounded by unknown constants  $c_1 > 0$  and  $c_2 > 0$ , i.e.,  $||v_l(t)|| \le c_1$ ,  $||\dot{v}_l(t)|| \le c_2$ ,  $\forall t \ge 0$ .

Assumption 3: At the initial time  $t_0 = 0$ , the following conditions  $m_{\min} \le m(t_0) \le m_{\max}$ ,  $\underline{n} \le n(t_0) \le n_{\max}$ ,  $d_j(t_0) > 0$ , and  $r_{j,i} > \underline{r}_i$ , j = 1, 2, are satisfied.

Remark 1: The initial conditions  $m_{\min} \leq m(t_0) \leq m_{\max}$  and  $\underline{n} \leq n(t_0) \leq n_{\max}$  mean that the target  $R_l$  is in the camera's FOV and collision-free with the follower  $R_f$ . The inequalities  $d_j(t_0) > 0$  imply that the visibility connectivity between the follower  $R_f$  and the target  $R_l$  is not occluded by obstacles. The conditions  $r_{j,f}(t_0) > \underline{r}_f$  mean that the follower  $R_f$  is collision-free with obstacles at the initial time.

Control Objective: Under Assumptions 1–3, given the desired pixel coordinate  $(m_d, n_d)$ , the control objective is to design an IBVS controller for the follower  $R_f$  such that the following conditions hold.

1) Visibility connectivity to the target  $R_l$  is always maintained and a collision with the target is avoided, that is, the constraint (10) is never violated.

2) The follower  $R_f$  can avoid collisions with obstacles, and when there is no obstacle detected, the tracking errors  $e_m$  and  $e_n$  converge to small neighborhoods of zero.

#### F. Preliminaries

Lemma 1 [26]: For two variables  $x, y \in \mathbb{R}$ , constants  $\varepsilon > 0$ , n > 1, and m > 1, if (n-1)(m-1) = 1, then the following inequality holds:

$$xy \le \frac{\varepsilon^n}{n} |x|^n + \frac{1}{m\varepsilon^m} |y|^m.$$

Lemma 2 [27]: For  $p = 1 + (1/\mu)$ ,  $q = 1 - (1/\mu)$  with a constant  $\mu > 1$ , and a variable  $x \ge 0$ , the following inequality holds:

$$-x^2 \le -x^p - x^q + 1.$$

*Lemma 3* [28]: For x > 0, i = 1, 2, ..., n, it follows:

$$\sum_{i=1}^{n} x_{i}^{p} \ge \left(\sum_{i=1}^{n} x_{i}\right)^{p}, \quad 0 
$$\sum_{i=1}^{n} x_{i}^{p} \ge n^{1-p} \left(\sum_{i=1}^{n} x_{i}\right)^{p}, \quad p > 1.$$$$

Lemma 4 [29]: For constants  $\alpha > 0$ ,  $\beta > 0$ , p > 1, and 0 < q < 1, if there exists a continuously radially unbounded and positive definite function V(x) such that  $\dot{V}(x) \leq -\alpha V^p(x) - \beta V^q(x)$ , then the origin of a system is globally fixed-time stable and the settling time function T can be estimated by

$$T \le T_{\max} := \frac{1}{\alpha (p-1)} + \frac{1}{\beta (1-q)}.$$

# III. IBVS CONTROL DESIGN

# A. Design of Constrained Boundary Functions

In order to tackle the obstacle-avoidance problem, the time-varying boundary constraints imposed on tracking errors are designed such that: 1) when there is no obstacle detected, the tracking errors can exponentially converge to small neighborhoods of zero and 2) when there is an obstacle on the neighborhood of the desired trajectory, the constrained boundary functions should increase or decrease accordingly to ensure the tracking errors to deviate from zero so that the following robot  $R_f$  diverges from its desired trajectory to avoid the obstacle without violating the boundary constraints.

The time-varying boundary constraints imposed on tracking errors are specified by

$$\beta_{mL}\left(t\right) < e_{m}\left(t\right) < \beta_{mH}\left(t\right), \quad \beta_{nL}\left(t\right) < e_{n}\left(t\right) < \beta_{nH}\left(t\right)$$
(14)

where  $\beta_*$ ,  $* \in \{mL, mH, nL, nH\}$ , are the constrained boundary functions to be specified later. For the purpose of designing constrained boundary functions that are suitable for obstacle avoidance, we need to clarify how the robot  $R_f$  should behave when obstacles are present. Since we only consider the two most dangerous obstacles, i.e.,  $O_1$  and  $O_2$ , at a time, the

obstacle-avoidance problem can be divided into the following two cases.

Case 1: There is only one obstacle  $(O_1 \text{ or } O_2)$ , tending to collide with robot  $R_f$ . In this scenario, obstacle avoidance is a higher priority rather than the tracking task, and thus, the follower  $R_f$  needs to perform a left or right turn to move away from the obstacle. To this end, the boundary functions  $\beta_{mL}$  and  $\beta_{mH}$  are designed to be adjustable according to the presence of obstacles, which guarantees the tracking errors deviate from zero such that  $R_f$  is driven to avoid the obstacle. In addition, robot  $R_f$  should turn more intensely for a greater overlap distance  $\rho_i$  since it needs more lateral displacement.

Case 2: The two obstacles  $O_1$  and  $O_2$  have potential to collide with robot  $R_f$ . This case happens when  $R_l$  is passing between  $O_1$  and  $O_2$ . According to Assumption 1, it is possible for  $R_f$  to pass between  $O_1$  and  $O_2$  and follow the target  $R_l$  without breaking visual connectivity. Therefore, robot  $R_f$ should first turn away from the closer obstacle, which is similar to Case 1, and then drive to a balanced spot between  $O_1$  and  $O_2$  where the need for turning left is equivalent to turning right. Meanwhile, robot  $R_f$  should get closer to  $R_l$  in order to pass through as soon as possible since this case is relatively more dangerous. This maneuver can be accomplished by decreasing the boundary functions  $\beta_{nL}$  and  $\beta_{nH}$  if h > 0.

Consider the FOV constraints (12) and (13) and time-varying boundary constraint (14), and the tracking errors  $e_m$  and  $e_n$  are required to satisfy the following conditions:

$$m_{\min} - m_d \le \beta_{mL}(t) < e_m(t) < \beta_{mH}(t) \le m_{\max} - m_d$$
(15)

$$\underline{n} - n_d \le \beta_{nL}(t) < e_n(t) < \beta_{nH}(t) \le n_{\text{max}} - n_d \quad (16)$$

which implies that the constrained boundary functions  $\beta_*$ ,  $* \in \{mL, mH, nL, nH\}$ , should be bounded. Motivated by the modifications of performance functions [20], we design the time derivatives of the constrained boundary functions by a Lipschitz continuous projection [20], [30] as follows:

$$\dot{\beta}_{*} = \begin{cases} \mu_{*}, & p(\beta_{*}) \leq 0\\ \mu_{*}, & p(\beta_{*}) \geq 0 \text{ and } \beta_{*}\mu_{*} \leq 0 \\ (1 - p(\beta_{*}))\mu_{*}, & \text{otherwise} \end{cases}$$
 (17)

with  $* \in \{mL, mH, nL, nH\}$ , where

$$\mu_{mL} = -\kappa_m \left( \beta_{mL} + \beta_{m,\infty} \right) + k_1 \left( \frac{f_2 e^{\kappa_p \rho_2}}{d_2 r_2} - \frac{f_1 e^{\kappa_p \rho_1}}{d_1 r_1} \right) \tag{18}$$

$$\mu_{mH} = -\kappa_m \left( \beta_{mH} - \beta_{m,\infty} \right) + k_1 \left( \frac{f_2 e^{\kappa_p \rho_2}}{d_2 r_2} - \frac{f_1 e^{\kappa_p \rho_1}}{d_1 r_1} \right)$$
(19)

$$\mu_{nL} = -\kappa_n \left( \beta_{nL} + \beta_{n,\infty} \right) - k_2 \left( 1 - f_{12} \right) \left( f_1 + f_2 \right) \tag{20}$$

$$\mu_{nH} = -\kappa_n \left( \beta_{nH} - \beta_{n,\infty} \right) - k_2 \left( 1 - f_{12} \right) \left( f_1 + f_2 \right) \tag{21}$$

$$p(\beta_*) = \frac{(\beta_* - \overline{\beta}_*)(\beta_* + \underline{\beta}_*)}{\epsilon^2 + \epsilon(\overline{\beta}_* + \underline{\beta}_*)}$$
(22)

in which

$$r_1 = r_{1,f} - \underline{r}_f, \quad r_2 = r_{2,f} - \underline{r}_f$$
 (23)

$$f_1 = f(\lambda_1, -\delta_{11}, \delta_{11}) - f(\lambda_1, 1, \delta_{12})$$
 (24)

$$f_2 = f(\lambda_2, -\delta_{21}, \delta_{21}) - f(\lambda_2, 1, \delta_{22})$$
 (25)

$$f_{12} = f(f_1 - f_2, 0, \delta_d) + f(f_2 - f_1, 0, \delta_d)$$
 (26)

$$f(x, a, b) = \frac{g(x - a)}{g(x - a) + g(b - x + a)}$$
(27)

$$f(x, a, b) = \frac{g(x - a)}{g(x - a) + g(b - x + a)}$$

$$g(x) = \begin{cases} 0, & x \le 0 \\ e^{-\frac{1}{x}}, & x > 0 \end{cases}$$
(27)

with  $\kappa_m$ ,  $\kappa_n$ ,  $\kappa_p$ ,  $k_1$ ,  $k_2$ ,  $\beta_{m,\infty}$ ,  $\beta_{n,\infty}$ ,  $\delta_{11}$ ,  $\delta_{12}$ ,  $\delta_{21}$ ,  $\delta_{22}$ , and  $\delta_d$  being positive design parameters. For a small constant  $\epsilon>0$ , the inequality  $-\epsilon+\underline{\beta}_*<\beta_*(t)<\overline{\beta}_*+\epsilon,*\in\{mL,mH,nL,nH\},\ \forall t\geq0$  is guaranteed by the Lipschitz continuous projection (17), where constants  $\beta_*$  and  $\overline{\beta}_*$  are the lower and upper bounds of the boundary functions  $\beta_*(t)$ , respectively. The use of the Lipschitz continuous projection (17) is to guarantee that the time-varying constrained boundary functions  $\beta_*$  remain within the camera's FOV, i.e.,

$$m_{\min} - m_d \le \beta_{mL}(t) < \beta_{mH}(t) \le m_{\max} - m_d \tag{29}$$

$$n - n_d < \beta_{nL}(t) < \beta_{nH}(t) < n_{\text{max}} - n_d$$
 (30)

hold by the proper choice of constant bounds of the boundary functions  $\beta_*(t)$ ,  $* \in \{mL, mH, nL, nH\}$ , where the constant bounds can be taken as

$$\underline{\beta}_{mL} = m_d - m_{\min} - \epsilon, \quad \overline{\beta}_{mL} = m_{\max} - m_d - 2\beta_{m,\infty} - \epsilon$$

$$\underline{\beta}_{mH} = m_d - m_{\min} - 2\beta_{m,\infty} - \epsilon, \quad \overline{\beta}_{mH} = m_{\max} - m_d - \epsilon$$

$$\underline{\beta}_{nL} = n_d - \underline{n} - \epsilon, \quad \overline{\beta}_{nL} = n_{\max} - n_d - 2\beta_{n,\infty} - \epsilon$$

$$\underline{\beta}_{nH} = n_d - \underline{n} - 2\beta_{n,\infty} - \epsilon, \quad \overline{\beta}_{nH} = n_{\max} - n_d - \epsilon. \quad (31)$$

We remark the following important observations for the design of constrained boundary functions.

Remark 2: Note that the first terms of  $\mu_*$ ,  $* \in$  $\{mL, mH, nL, nH\}$  given in (18)–(21), are the time derivatives of performance functions [21], [24], which are taken as the exponentially decaying functions of time, and thus, the first terms of  $\mu_*$  define the behaviors of the constrained boundary functions when there is no obstacle detected, where  $\kappa_m$  and  $\kappa_n$  are their exponentially decaying rates and  $\beta_{*,\infty}$  are their steady-state boundaries.

Remark 3: When robot  $R_f$  approaches an obstacle, we have  $r_1 \rightarrow 0$  or/and  $r_2 \rightarrow 0$  by (23). Moreover,  $d_1r_1 \rightarrow 0$  $(d_2r_2 \rightarrow 0)$  means that the obstacle is on the left (right) side of robot  $R_f$ . It follows from (18) and (19) that as  $d_1r_1 \rightarrow 0$ , we have  $\mu_{mL} \to -\infty$  and  $\mu_{mH} \to -\infty$ , which implies that  $\dot{\beta}_*$  given in (17) is negative. As a result, the values of the constrained boundary functions  $\beta_*$  are decreased, which drives the feature point in the pixel coordinate to deviate from its desired value to the right side, and then, robot  $R_f$  turns right to avoid the obstacle on its left side. Similarly, when  $d_2r_2 \rightarrow 0$ , the constrained boundary functions  $\beta_*$  will drive robot  $R_f$  turns left to avoid the obstacle on its right side.

Remark 4:  $f(x,a,b): \mathbb{R} \to [0,1]$  given in (27) is a smooth and differentiable function. As shown in Fig. 3, f(x, a, b) = 0 for  $x \le a$ , and f(x, a, b) = 1 for  $x \ge a + b$ . When a < x < a + b, f(x, a, b) varies from 0 to 1.  $f_1$ ,  $f_2$ , and  $f_{12}$  given in (24)–(26) are activation functions that activate different obstacle-avoidance behaviors. More specifically, in Case 1, robot  $R_f$  needs to perform a turn to avoid the obstacle. When the obstacle  $O_i$  lies between the target  $R_l$ 

and the follower  $R_f$ , i.e.,  $0 < \lambda_j < 1$ , the activation function  $f_1$  or  $f_2$  is active with  $0 < f \le 1$ . If  $f_1$  is active, then robot  $R_f$  turns right to avoid the obstacle on the left. If  $f_2$  is active, then  $R_f$  turns left to avoid the obstacle on the right. Moreover, the terms  $e^{\kappa_p \rho_j}$ ,  $j = \{1, 2\}$ , presented in (18) and (19) are introduced as scaling factors for  $f_j$  to adjust turning intensity according to the overlap distance  $\rho_j$  shown in Fig. 1. In Case 2, both  $f_1$  and  $f_2$  are active, which implies that robot  $R_f$  needs to turn left and right at the same time. When the need for turning left is equivalent to turning right, robot  $R_f$  reaches a balanced spot and stops turning. Note that  $(1 - f_{12})$  is active in Case 2 only, which leads to decrement of  $\beta_{nL}$  and  $\beta_{nH}$ , and then, the following robot  $R_f$  eventually gets closer to the target  $R_l$  if h > 0.

Remark 5: The design parameters  $k_1$ ,  $k_2$ , and  $\kappa_p$  determine how intensely robot  $R_f$  would turn left or right under the same  $d_j r_j$  and  $\rho_j$ ,  $j=\{1,2\}$ . The bigger they are, more intense the turn is. The design parameters  $\delta_*$ ,  $*\in\{11,12,21,22,d\}$ , are used to adjust when and how rapidly  $f_1$ ,  $f_2$ , and  $f_{12}$  activate and deactivate. With larger design parameters  $\delta_*$ , the corresponding activation functions activate and deactivate more slowly, and the obstacle avoidance would begin earlier and end later. Therefore, larger  $\delta_*$  are preferred in practice such that the robot  $R_f$  can smoothen abrupt turns. However,  $\delta_*$  are also limited by the sensing range of onboard radar or LiDAR.

## B. Control Design

To solve the vision-based tracking control problem for the following robot  $R_f$ , we impose FOV and time-varying boundary constraints to ensure visibility connectivity to the moving target and there is no collision with the target or obstacles simultaneously. To be more specific, in this section, we first introduce an error transformation, then contract the dynamics of the constrained boundary functions based on the obstacle-avoidance behavior and constraint (10), and finally construct a tracking controller to keep  $e_m$  and  $e_n$  between their corresponding constrained boundary functions, which leads to provable visibility maintenance and collision avoidance.

Define the following error transformation variable:

$$\eta_s = \ln\left(\frac{e_s - \beta_{sL}}{\beta_{sH} - e_s}\right), \quad s \in \{m, n\}.$$
 (32)

Taking the time derivative of  $[\eta_m, \eta_n]^T$  along system (8) and (11) yields

$$\begin{bmatrix} \dot{\eta}_m \\ \dot{\eta}_n \end{bmatrix} = G \begin{bmatrix} \frac{1}{h} & 0 \\ 0 & 1 \end{bmatrix} \begin{bmatrix} v_f \\ \omega_f \end{bmatrix} + \frac{qv_l}{h} H + \begin{bmatrix} \xi_1 \\ \xi_2 \end{bmatrix}$$
(33)

where

$$\xi_{1} = \frac{\partial \eta_{m}}{\partial \beta_{mL}} \dot{\beta}_{mL} + \frac{\partial \eta_{m}}{\partial \beta_{mH}} \dot{\beta}_{mH}, \quad \xi_{2} = \frac{\partial \eta_{n}}{\partial \beta_{nL}} \dot{\beta}_{nL} + \frac{\partial \eta_{n}}{\partial \beta_{nH}} \dot{\beta}_{nH}$$

$$G = \begin{bmatrix} \frac{\partial \eta_{m}}{\partial e_{m}} q (m_{0} - m) & \frac{\partial \eta_{m}}{\partial e_{m}} [a_{m} + (m - m_{0}) p] \\ \frac{\partial \eta_{n}}{\partial e_{n}} q (n_{0} - n) & \frac{\partial \eta_{n}}{\partial e_{n}} (n - n_{0}) p \end{bmatrix}$$

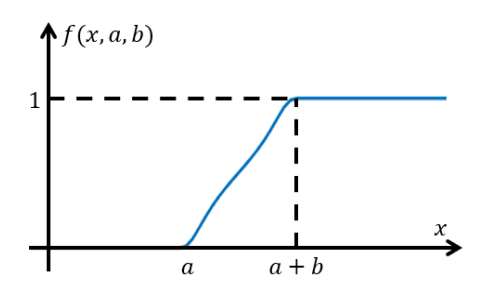


Fig. 3. Schematics of the design function f(x, a, b) given in (27).

$$H = \begin{bmatrix} \frac{\partial \eta_m}{\partial e_m} \left[ a_m \sin \theta_{lf} + (m - m_0) \cos \theta_{lf} \right] \\ \frac{\partial \eta_n}{\partial e_n} (n - n_0) \cos \theta_{lf} \end{bmatrix}.$$

Although  $\theta_l$  cannot be directly obtained as a feedback signal, the relative orientation  $\theta_{lf}$  can be computed by the homography-based technique given in [31] with visual feedback information. More specifically, we can obtain  $\theta_{lf}$  by the Euclidean homography reconstruction if there are at least four available coplanar feature points on the target. If the displacements between the feature points are known, then the number of the feature points can be reduced to three using the pose estimate method. If there are not enough coplanar feature points on the target, we can still employ the virtual parallax algorithm presented in [31] to calculate  $\theta_{lf}$  with eight random feature points. Hence,  $\theta_{lf}$  is available for feedback control design and  $\theta_l$  can be computed by  $\theta_l = \theta_{lf} + \theta_f$ .

Since system (33) contains the uncertain feature height h and the unknown target's velocity  $\vartheta_l = v_l/h$ , we cannot directly introduce them into the control inputs. To compensate for these unknown variables, we employ an adaptive estimator and a velocity observer to estimate h and  $\vartheta_l$ , respectively. Define the estimation errors  $\tilde{h} = \hat{h} - h$  and  $\tilde{\vartheta}_l = \hat{\vartheta}_l - \vartheta_l$ , where  $\hat{h}$  and  $\hat{\vartheta}_l$  are the estimations of h and  $\vartheta_l$ , respectively.

Consider the following BLF candidate:

$$V = \frac{1}{2} \eta^T \eta + \frac{1}{2\nu_1 h} \tilde{h}^2 + \frac{1}{2\nu_2} \tilde{\vartheta}_l^2$$
 (34)

with  $\eta = [\eta_m, \eta_n]^T$ , where  $\gamma_1 > 0$  and  $\gamma_2 > 0$  are design parameters. The time derivative of (34) along system (33) is given by

$$\dot{V} = \boldsymbol{\eta}^T G \begin{bmatrix} \frac{1}{h} & 0 \\ 0 & 1 \end{bmatrix} \begin{bmatrix} v_f \\ \omega_f \end{bmatrix} + \boldsymbol{\eta}^T q \vartheta_l H + \boldsymbol{\eta}^T \begin{bmatrix} \xi_1 \\ \xi_2 \end{bmatrix} + \frac{1}{\gamma_1 h} \tilde{h} \dot{\hat{h}} + \frac{1}{\gamma_2} \tilde{\vartheta}_l (\dot{\hat{\vartheta}}_l - \dot{\vartheta}_l).$$
(35)

Hence, the IBVS control inputs  $v_f$  and  $\omega_f$  given in system (33) can be taken as

$$\begin{bmatrix} v_f \\ \omega_f \end{bmatrix} = \begin{bmatrix} \hat{h} & 0 \\ 0 & 1 \end{bmatrix} G^{-1} \Gamma \tag{36}$$

in which the adaptive law and the velocity observer are designed as follows:

$$\dot{\hat{h}} = -\gamma_1 \boldsymbol{\eta}^T G \begin{bmatrix} 1 & 0 \\ 0 & 0 \end{bmatrix} G^{-1} \Gamma - \sigma_1 \hat{h}^3$$
 (37)

$$\dot{\hat{\vartheta}}_l = \gamma_2 \boldsymbol{\eta}^T q H - \hat{\vartheta}_l - \sigma_2 \hat{\vartheta}_l^3 \tag{38}$$

with  $\Gamma = -K_1 \operatorname{sig}(\boldsymbol{\eta})^{(3/2)} - K_2 \operatorname{sig}(\boldsymbol{\eta})^{(1/2)} - q \hat{\vartheta}_l H - [\xi_1, \xi_2]^T$ , where  $\sigma_1 > 0$ ,  $\sigma_2 > 0$ ,  $K_1 > 0$ , and  $K_2 > 0$  are design parameters, and  $\operatorname{sig}(\boldsymbol{x})^a \triangleq [\operatorname{sig}(x_1)^a, \operatorname{sig}(x_2)^a, \cdots, \operatorname{sig}(x_n)^a]^T$ .  $\operatorname{sig}(x)^a = \operatorname{sgn}(x)|x|^a$  is a continuous function with a > 0 and  $x \in \mathbb{R}$ . Note that  $\det(G) = -(\partial \eta_m/\partial e_m)(\partial \eta_n/\partial e_n)a_mq(n_0 - n) \neq 0$  due to  $(\partial \eta_m/\partial e_m) \neq 0$ ,  $(\partial \eta_n/\partial e_n) \neq 0$ , and  $n_0 - n = a_nh/x_{p,f} > 0$ , and thus, the matrix G defined in (33) is invertible.

Substituting (36)–(38) into (35) gives

$$\dot{V} = -\boldsymbol{\eta}^T K_1 \operatorname{sig}(\boldsymbol{\eta})^{\frac{3}{2}} - \boldsymbol{\eta}^T K_2 \operatorname{sig}(\boldsymbol{\eta})^{\frac{1}{2}} - \frac{1}{\gamma_2} \tilde{\vartheta}_l \hat{\vartheta}_l - \frac{1}{\gamma_2} \tilde{\vartheta}_l \dot{\vartheta}_l 
- \frac{\sigma_1}{\gamma_1 h} \tilde{h} \left( \tilde{h}^3 + 3\tilde{h}^2 h + 3\tilde{h}h^2 + h^3 \right) 
- \frac{\sigma_2}{\gamma_2} \tilde{\vartheta}_l \left( \tilde{\vartheta}_l^3 + 3\tilde{\vartheta}_l^2 \vartheta_l + 3\tilde{\vartheta}_l \vartheta_l^2 + \vartheta_l^3 \right).$$
(39)

By the completion of squares, we have

$$\begin{split} & -\tilde{h}h^3 \leq 3\tilde{h}^2h^2 + \frac{1}{12}h^4, \quad -\tilde{\vartheta}_l\vartheta_l^3 \leq 3\tilde{\vartheta}_l^2\vartheta_l^2 + \frac{1}{12}\vartheta_l^4 \\ & -\tilde{\vartheta}_l\hat{\vartheta}_l \leq -\frac{1}{2}\tilde{\vartheta}_l^2 + \frac{1}{2}\vartheta_l^2, \quad -\tilde{\vartheta}_l\dot{\vartheta}_l \leq \frac{1}{2}\tilde{\vartheta}_l^2 + \frac{1}{2}\dot{\vartheta}_l^2. \end{split}$$

Then, we obtain

$$\dot{V} \leq -\eta^{T} K_{1} \operatorname{sig}(\eta)^{\frac{3}{2}} - \eta^{T} K_{2} \operatorname{sig}(\eta)^{\frac{1}{2}} + \frac{1}{2\gamma_{2}} \vartheta_{l}^{2} + \frac{1}{2\gamma_{2}} \dot{\vartheta}_{l}^{2} 
- \frac{\sigma_{1}}{\gamma_{1}h} \tilde{h}^{4} - \frac{3\sigma_{1}}{\gamma_{1}h} \tilde{h}^{3}h + \frac{\sigma_{1}}{12\gamma_{1}h} h^{4} 
- \frac{\sigma_{2}}{\gamma_{2}} \tilde{\vartheta}_{l}^{4} - \frac{3\sigma_{2}}{\gamma_{2}} \tilde{\vartheta}_{l}^{3} \vartheta_{l} + \frac{\sigma_{2}}{12\gamma_{2}} \vartheta_{l}^{4}.$$
(40)

Applying Lemma 1 to  $-\tilde{h}^3h$  and  $-\tilde{\vartheta}_l^3\vartheta_l$  in (40) with  $\varepsilon > 0$ , n = (4/3), m = 4, and ((4/3) - 1)(4 - 1) = 1, we obtain

$$\dot{V} \leq -\boldsymbol{\eta}^{T} K_{1} \operatorname{sig}(\boldsymbol{\eta})^{\frac{3}{2}} - \boldsymbol{\eta}^{T} K_{2} \operatorname{sig}(\boldsymbol{\eta})^{\frac{1}{2}} + \frac{1}{2\gamma_{2}} \vartheta_{l}^{2} + \frac{1}{2\gamma_{2}} \dot{\vartheta}_{l}^{2} 
- \left(\frac{\sigma_{1}}{\gamma_{1}h} - \frac{9\varepsilon^{\frac{4}{3}}\sigma_{1}}{4\gamma_{1}h}\right) \tilde{h}^{4} + \left(\frac{3\sigma_{1}}{4\varepsilon^{4}\gamma_{1}h} + \frac{\sigma_{1}}{12\gamma_{1}h}\right) h^{4} 
- \left(\frac{\sigma_{2}}{\gamma_{2}} - \frac{9\varepsilon^{\frac{4}{3}}\sigma_{2}}{4\gamma_{2}}\right) \tilde{\vartheta}^{4} + \left(\frac{3\sigma_{2}}{4\varepsilon^{4}\gamma_{2}} + \frac{\sigma_{2}}{12\gamma_{2}}\right) \vartheta_{l}^{4} \tag{41}$$

with  $((\sigma_1/\gamma_1 h) - (9\varepsilon^{(4/3)}\sigma_1/4\gamma_1 h)) > 0$  and  $((\sigma_2/\gamma_2) - (9\varepsilon^{(4/3)}\sigma_2/4\gamma_2)) > 0$ . Under Assumption 2, using Lemma 2 with  $x = \tilde{h}^2$ ,  $\tilde{\vartheta}^2$  given in (41), and  $\mu = 4$ , it follows:

$$\dot{V} \leq -\boldsymbol{\eta}^{T} K_{1} \operatorname{sig}(\boldsymbol{\eta})^{\frac{3}{2}} - \boldsymbol{\eta}^{T} K_{2} \operatorname{sig}(\boldsymbol{\eta})^{\frac{1}{2}} \\
-\left(\frac{\sigma_{1}}{\gamma_{1}h} - \frac{9\varepsilon^{\frac{4}{3}}\sigma_{1}}{4\gamma_{1}h}\right) \left|\tilde{h}\right|^{\frac{5}{2}} \\
-\left(\frac{\sigma_{1}}{\gamma_{1}h} - \frac{9\varepsilon^{\frac{4}{3}}\sigma_{1}}{4\gamma_{1}h}\right) \left|\tilde{h}\right|^{\frac{3}{2}} - \left(\frac{\sigma_{2}}{\gamma_{2}} - \frac{9\varepsilon^{\frac{4}{3}}\sigma_{2}}{4\gamma_{2}}\right) \left|\tilde{\vartheta}_{l}\right|^{\frac{5}{2}} \\
-\left(\frac{\sigma_{2}}{\gamma_{2}} - \frac{9\varepsilon^{\frac{4}{3}}\sigma_{2}}{4\gamma_{2}}\right) \left|\tilde{\vartheta}_{l}\right|^{\frac{3}{2}} + \Delta \tag{42}$$

where  $\Delta = ((\sigma_1/\gamma_1 h) - (9\varepsilon^{(4/3)}\sigma_1/4\gamma_1 h)) + ((\sigma_2/\gamma_2) - (9\varepsilon^{(4/3)}\sigma_2/4\gamma_2)) + ((3\sigma_1/4\varepsilon^4\gamma_1 h) + (\sigma_1/12\gamma_1 h))h^4 + ((3\sigma_2/4\varepsilon^4\gamma_2) + (\sigma_2/12\gamma_2))(c_1^4/h^4) + (c_1^2/2\gamma_2 h^2) +$ 

 $(c_2^2/2\gamma_2h^2) > 0$  is a constant. From (42) and Lemma 3, it follows that:

$$\dot{V} \le -\alpha V^{\frac{5}{4}} - \beta V^{\frac{3}{4}} + \Delta \tag{43}$$

in which  $\alpha = \min\{4((2/4))^{(5/4)}k_{m1}, 4((2\gamma_1h/4))^{(5/4)} ((\sigma_1/\gamma_1h) - (9\varepsilon^{(4/3)}\sigma_1/4\gamma_1h)), 4((2\gamma_2/4))^{(5/4)}((\sigma_2/\gamma_2) - (9\varepsilon^{(4/3)}\sigma_2/4\gamma_2))\}, \beta = \min\{2^{(3/4)}k_{m2}, (2\gamma_1h)^{(3/4)}((\sigma_1/\gamma_1h) - (9\varepsilon^{(4/3)}\sigma_1/4\gamma_1h)), (2\gamma_2)^{(3/4)}((\sigma_2/\gamma_2) - (9\varepsilon^{(4/3)}\sigma_2/4\gamma_2))\}, \text{ and } k_{m1} \text{ and } k_{m2} \text{ are the minimum eigenvalues of } K_1 \text{ and } K_2, \text{ respectively.}$ 

## C. Stability Analysis

The following theorem shows that the proposed IBVS controller achieves the fixed-time convergence of tracking errors while guaranteeing visibility maintenance and obstacle/collision avoidance.

Theorem 1: Under Assumptions 1–3, consider system (8) and IBVS tracking controller (36) with adaptive law (37) and velocity observer (38), then we have the following results.

1) The tracking errors  $e_m$  and  $e_n$  converge to the following compact sets:

$$\Omega_{e_m} = \left\{ e_m \middle| \underline{e}_m \le e_m \le \overline{e}_m \right\} \tag{44}$$

$$\Omega_{e_n} = \left\{ e_n \middle| \underline{e}_n \le e_n \le \overline{e}_n \right\} \tag{45}$$

in the fixed time  $T \leq T_{\text{max}} = (4/\alpha \overline{\omega}) + (4/\beta)$  with  $\overline{\omega} \in (0, 1)$ , in which  $\underline{e}_m$ ,  $\overline{e}_m$ ,  $\underline{e}_n$ , and  $\overline{e}_n$  are given by

$$\begin{split} \underline{e}_{m} &= \frac{\beta_{mL} + \beta_{mH}}{2} - \frac{(e^{\chi} - 1)(\beta_{mH} - \beta_{mL})}{2(1 + e^{\chi})} \\ \overline{e}_{m} &= \frac{\beta_{mL} + \beta_{mH}}{2} + \frac{(e^{\chi} - 1)(\beta_{mH} - \beta_{mL})}{2(1 + e^{\chi})} \\ \underline{e}_{n} &= \frac{\beta_{nL} + \beta_{nH}}{2} - \frac{(e^{\chi} - 1)(\beta_{mH} - \beta_{mL})}{2(1 + e^{\chi})} \\ \overline{e}_{n} &= \frac{\beta_{nL} + \beta_{nH}}{2} + \frac{(e^{\chi} - 1)(\beta_{nH} - \beta_{nL})}{2(1 + e^{\chi})} \end{split}$$

where the constant  $\chi$  can be made arbitrarily small by increasing the controller gain  $k_{m1}$  and the design parameters  $\gamma_1$  and  $\gamma_2$ . Note that the desired obstacle-avoidance trajectory  $(((\beta_{mL} + \beta_{mH})/2), ((\beta_{nL} + \beta_{nH})/2))$  depends on the constrained boundary functions  $\beta_*(t)$ ,  $* \in \{mL, mH, nL, nH\}$ . In particular, when there is no obstacle, the pixel coordinate tracking error  $(e_m, e_n)$  will converge to a small neighborhood of zero in the fixed time  $T \leq T_{\text{max}}$ .

- 2) The following robot  $R_f$  never breaks the visibility connection and never collides with the target  $R_l$  and obstacles during the whole operation, that is, the constraint conditions (15) and (16) with (17) and (31) are guaranteed.
- All signals in the closed-loop system are uniformly ultimately bounded.

*Proof:* The following conditions hold.

1) Inequality (43) can be rewritten as

$$\dot{V} \le -\overline{\omega}\alpha V^{\frac{5}{4}} - \beta V^{\frac{3}{4}} - (1 - \overline{\omega})\alpha V^{\frac{5}{4}} + \Delta. \tag{46}$$

From (46), it is clear that  $\dot{V} \leq -\overline{\omega}\alpha V^{(5/4)} - \beta V^{(3/4)}$  for  $V \geq ((\Delta/(\alpha(1-\overline{\omega}))))^{(4/5)}$ , which indicates that

V would converge to the set given by  $\{V: V \leq ((\Delta/(\alpha(1-\overline{\omega}))))^{(4/5)}\}$  in fixed time according to Lemma 4. Moreover, the maximum convergence time can be estimated by  $T_{\max} = (4/\alpha\overline{\omega}) + (4/\beta)$ . Recalling (34), we have

$$\frac{1}{2}\boldsymbol{\eta}^{T}\boldsymbol{\eta} + \frac{1}{2\gamma_{1}h}\tilde{h}^{2} + \frac{1}{2\gamma_{2}}\tilde{\vartheta}_{l}^{2} \leq \left(\frac{\Delta}{\alpha(1-\overline{\omega})}\right)^{\frac{4}{5}} \tag{47}$$

for  $t \geq T_{\text{max}}$ , which indicates that  $\eta_m$  and  $\eta_n$  satisfy

$$|\eta_m| \le \chi, \quad |\eta_n| \le \chi, \quad \chi = \sqrt{2\left(\frac{\Delta}{\alpha (1-\overline{\omega})}\right)^{\frac{4}{5}}}$$
(48)

where  $\chi$  can be made arbitrarily small by increasing the controller gain  $k_{m1}$  and the design parameters  $\gamma_1$  and  $\gamma_2$ . From (32) and (48), it follows that tracking errors  $e_m$  and  $e_n$  converge to the compact sets  $\Omega_{e_m}$  and  $\Omega_{e_n}$  given in (44) and (45), respectively. When there is no obstacle around, it follows  $\beta_{mL} \to -\beta_{m,\infty}$ ,  $\beta_{mH} \to \beta_{m,\infty}$ ,  $\beta_{nL} \to -\beta_{n,\infty}$ , and  $\beta_{nH} \to \beta_{n,\infty}$ , which means that  $e_m$  and  $e_n$  converge to small neighborhoods of zero in the fixed time  $T \leq T_{\text{max}}$ .

- 2) Next, we show that there is no collision with obstacles during the whole motion operation. Consider Cases 1 and 2 presented in Section III-A. For Case 1, assume that the obstacle is  $O_1$ . When robot  $R_f$  approaches the obstacle  $O_1$ , we have  $(1/d_1r_1) \rightarrow +\infty$  and  $(1/d_2r_2)$ is bounded, which means that the proposed controller takes  $O_1$  into account only. This leads to  $R_f$  moving away from  $O_1$  immediately, resulting in an increment of  $d_1r_1$ . Thus,  $d_1r_1 > 0$  holds while avoiding  $O_1$ . The same arguments hold when the obstacle is  $O_2$ . For Case 2, both  $f_1$  and  $f_2$  are active. For the worst case scenario, we have that both  $d_1r_1$  and  $d_2r_2$  tend to 0. For this case, the first terms of  $\mu_{mL}$  and  $\mu_{mH}$  can be neglected since  $((f_1e^{\kappa_p\rho_1})/d_1r_1)$  and  $((f_2e^{\kappa_p\rho_2})/d_2r_2)$ tend to  $+\infty$ . As a result, robot  $R_f$  will turn away from the obstacle that has bigger  $(e^{\kappa_p \rho_j}/d_i r_i)$ , j = 1, 2, and stop turning when  $(e^{\kappa_p \rho_1}/d_1 r_1)$  and  $(e^{\kappa_p \rho_2}/d_2 r_2)$ are balanced. Consequently, both  $d_1r_1$  and  $d_2r_2$  can be kept away from zero, which indicates that  $R_f$ would navigate through obstacles with no collision. Therefore, it is concluded that  $R_f$  can always avoid collision with obstacles and occlusion during the operation under Assumption 1. It follows from (32) that  $e_s = ((e^{\eta_s} \beta_{sH} + \beta_{sL})/(1 + e^{\eta_s})), s \in \{m, n\}.$  Note that  $e_s$  is strictly increasing with respect to  $\eta_s$ , and thus, we have  $e_s \to \beta_{sH}$  if and only if (iff)  $\eta_s \to -\infty$ , and  $e_s \to \beta_{sL}$  iff  $\eta_s \to +\infty$ . Since the boundedness of  $\eta_s$ , we have  $\beta_{sL} < e_s < \beta_{sH}$ , which indicates that constraint (14) is never violated. For the choice of the lower and upper bounds  $\beta_*$  and  $\overline{\beta}_*$  given in (31), inequalities (29) and (30) hold. Hence, constraint conditions (15) and (16) are satisfied since constraints (14), (29), and (30) are never violated.
- 3) It follows from (47) that  $\eta_m$ ,  $\eta_n$ ,  $\tilde{h}$ , and  $\tilde{\vartheta}_l$  are uniformly ultimately bounded. Furthermore, it is concluded

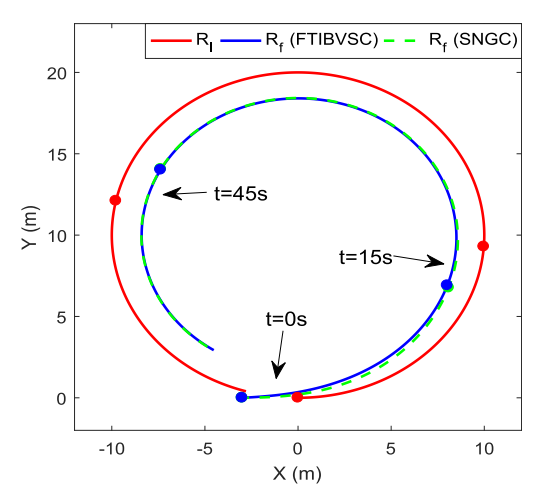


Fig. 4. Phase-plane trajectories of the two robots for no obstacle scenario using the proposed FTIBVSC (blue) and the existing SNGC [19] (green).

that the constrained boundary functions and their time derivatives are always bounded since neither a collision with obstacles nor an occlusion would occur according to proof 2). Consequently, all signals  $v_f$ ,  $\hat{h}$ , and  $\hat{\vartheta}_l$  in the closed-loop system are uniformly ultimately bounded. This completes the proof.

Remark 6: To achieve a high tracking performance, it can be seen from (48) that a small value of  $\chi$  is preferred. Hence, in view of (42) and (43), a small  $\Delta$  and a large  $\alpha$  are desirable, which requires a large control gain  $k_{m1}$  and large design parameters  $\gamma_1$  and  $\gamma_2$ . Furthermore, it follows from (44) and (45) that the pixel coordinate tracking error  $(e_m, e_n)$  can converge to a small neighborhood of the desired obstacle-avoidance trajectory  $(((\beta_{mL} + \beta_{mH})/2), ((\beta_{nL} + \beta_{nH})/2))$  in the fixed time  $T \leq T_{\text{max}}$ , where the desired obstacle-avoidance trajectory is generated from the center orbit of the constrained boundary functions  $\beta_*(t)$ ,  $*\in\{mL, mH, nL, nH\}$ . When there is no obstacle detected, we have  $\beta_{mL} \rightarrow -\beta_{m,\infty}$ ,  $\beta_{mH} \rightarrow \beta_{m,\infty}$ ,  $\beta_{nL} \rightarrow -\beta_{n,\infty}$ , and  $\beta_{nH} \rightarrow \beta_{n,\infty}$ , which means that the desired obstacle-avoidance trajectory converges to the origin.

# IV. COMPARATIVE SIMULATION STUDIES

To show the improved control performance of the proposed fixed-time IBVS controller (FTIBVSC), we perform comparative simulation studies between the proposed control law (36) and the static nonlinear gain controller (SNGC) recently presented in [19] for two scenarios where there are no obstacle and four obstacles in the workspace. The SNGC [19] is chosen here due to the fact that it is the most relatively related work, to the best of our knowledge, and is one of the state-of-the-art methods for IBVS tracking control of mobile robots with FOV constraints. In the simulations, the visual feedback information is obtained by a virtual camera, which is implemented according to (6). The resolution of the virtual camera is 640 × 480. The intrinsic matrix is given by

$$A = \begin{bmatrix} 376.1587 & 0 & 320 \\ 0 & 376.1587 & 240 \\ 0 & 0 & 1 \end{bmatrix}.$$

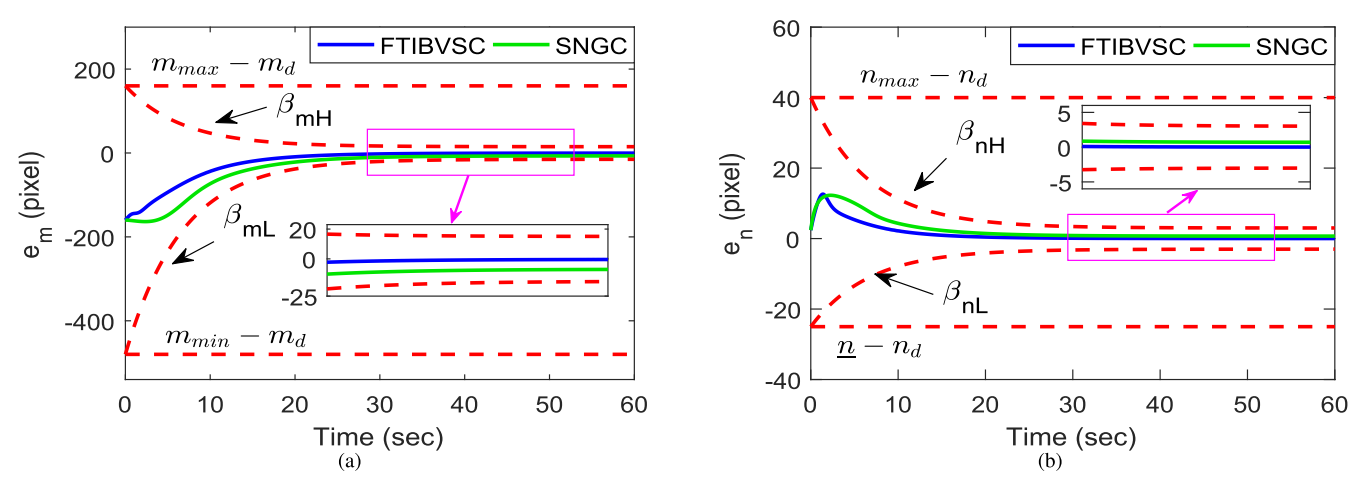


Fig. 5. Evolutions of tracking errors for no obstacle scenario using the proposed FTIBVSC (36) (blue) and the existing SNGC [19] (green): (a) tracking error  $e_m$  and (b) tracking error  $e_n$ .

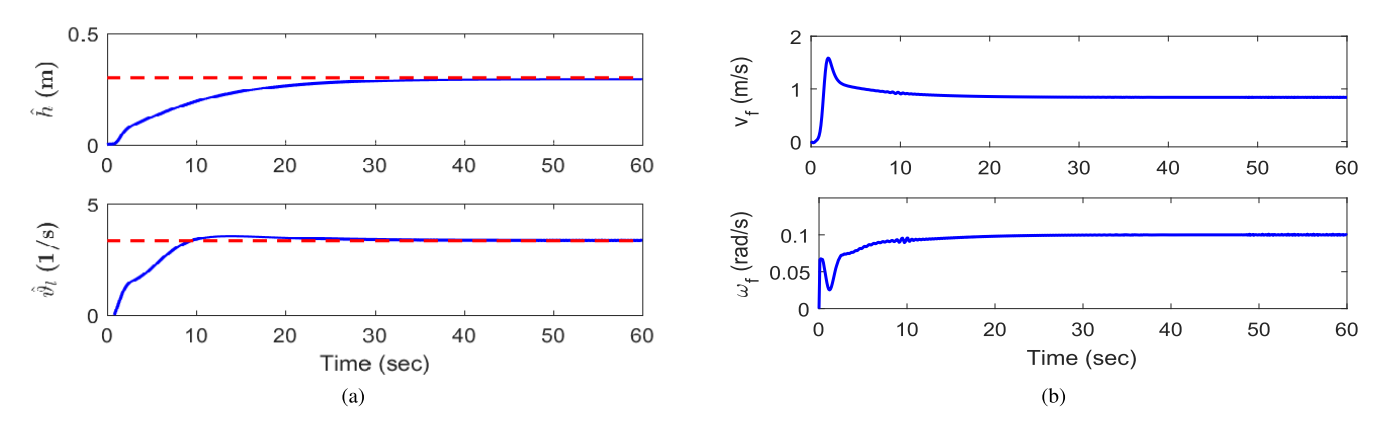


Fig. 6. (a) Estimations of h and  $\vartheta_l$  by (37) and (38). (b) Velocity inputs of  $R_f$  given by (36).

The radii of the safe zones of robots  $R_l$  and  $R_f$  are  $\underline{r}_l = \underline{r}_f = 0.8$  m. The feature height is h = 0.3 m. The desired pixel coordinate of the feature point is  $[480, 200]^T$ . The constraint (10) is specified by  $0 \le m \le 640$ ,  $169.4702 \le n \le 480$ . The design parameters of the constrained boundary functions are taken as  $\kappa_m = \kappa_n = 0.15$ ,  $\kappa_p = 2$ ,  $k_1 = 40$ ,  $k_2 = 0.1$ ,  $\delta_{11} = 1.8$ ,  $\delta_{21} = 1$ ,  $\delta_{12} = \delta_{22} = 0.2$ ,  $\delta_d = 5$ ,  $\beta_{m,\infty} = 15$ ,  $\beta_{n,\infty} = 3$ ,  $\beta_{mL}(0) = -480$ ,  $\beta_{mH}(0) = 160$ ,  $\beta_{nL}(0) = -25$ ,  $\beta_{nH}(0) = 40$ , and  $\epsilon = 2$ . Let  $\beta_{mL} = 478$ ,  $\beta_{mL} = 128$ ,  $\beta_{mH} = 448$ ,  $\beta_{mH} = 158$ ,  $\beta_{nL} = 23$ ,  $\beta_{nL} = 32$ ,  $\beta_{nH} = 17$ , and  $\beta_{nH} = 38$ . Thus, we have

$$-480 \le \beta_{mL}(t) < \beta_{mH}(t) \le 160$$
  
-25 \le \beta\_{nL}(t) < \beta\_{nH}(t) \le 40.

In the following simulations, we consider two scenarios where there are no obstacle and four obstacles in the workspace.

Case I: First, we consider the scenario where there is no obstacle in the workspace. The velocity inputs of the target  $R_l$  are set to be  $v_l = 1$  m/s and  $\omega_l = 0.1$  rad/s, and the initial pose of  $R_l$  is  $[0,0,0]^T$ . The initial states of the following robot  $R_f$  are  $[x_f(0), y_f(0), \theta_f(0)]^T = [-3, 0, 0]^T$  and  $v_f(0) = \omega_f(0) = 0$ . The control gain matrices of the proposed controller are taken as  $K_1 = \text{diag}(3, 10)$  and  $K_2 = \text{diag}(0.5, 3)$ . The adaptive gains are chosen as  $\gamma_1 = 0.02$  and

 $\sigma_1 = 0.25$ . The observer gains are set to be  $\gamma_2 = 23$  and  $\sigma_2 = 0.01$ . The control gains for the SNGC in [19] are given by  $k_1 = -0.1$  and  $k_2 = 2$ . The simulation results for Case I are shown in Figs. 4-6. Fig. 4 shows the trajectories of the two mobile robots and their positions at 0, 15, and 45 s. It can be seen from Figs. 4 and 5 that both the proposed controller (36) and the SNGC [19] can satisfy constraint (14) and the tracking errors converge to small regions around zero. Compared with the tracking errors shown in Fig. 5, larger tracking errors are caused using the SNGC [19] in the transient and steady-state stages. This is mainly because there is no compensation for the uncertain parameter h and the target's velocity  $v_l$  in the static nonlinear gain (SNG) control inputs [19]. On the contrary, we employ an adaptive estimator to estimate the unknown constant h and present a velocity observer to estimate the target's velocity  $v_l$ , whose effectiveness is well demonstrated in Fig. 6(a), and then, the estimates of h and  $v_l$  are embedded in the proposed control inputs (36) such that smaller tracking errors are achieved. Furthermore, it can be seen from Fig. 5 that the convergence speed of tracking errors is improved because the fixed-time convergence property is applied in the proposed IBVS controller (36). The velocity inputs of  $R_f$  using the proposed controller are shown in Fig. 6(b).

Case II: In this case, the mobile robots are operating in an obstacle environment. The velocity inputs of the target  $R_l$  are

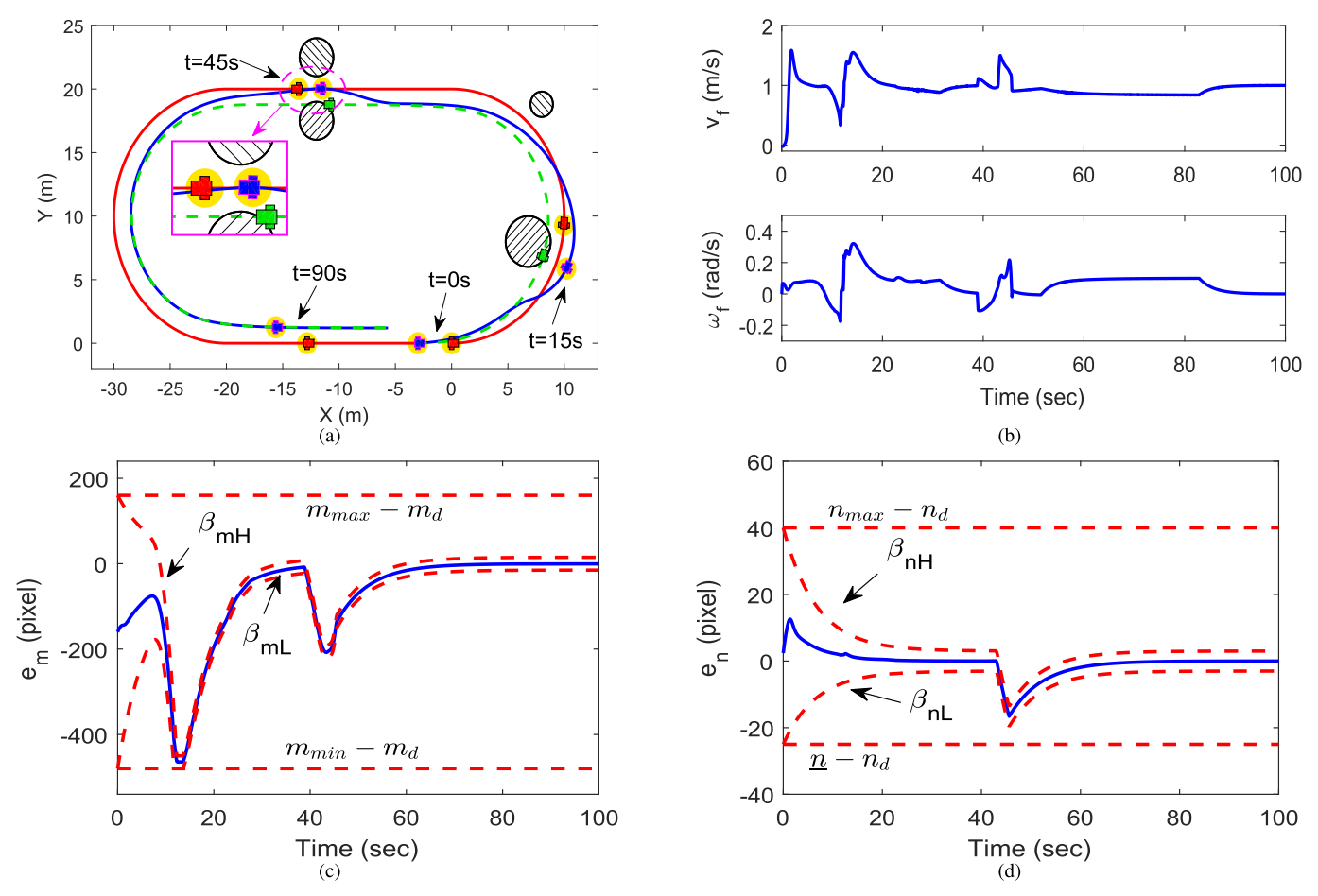


Fig. 7. Responses of the proposed IBVS controller and the existing SNGC [19] for the case when there are four obstacles in the workspace. (a) Phase-plane trajectories of the two robots:  $R_l$  (red solid line) and  $R_f$  using the proposed IBVS controller (blue solid line) and  $R_f$  using the existing SNGC [19] (green dashed line). (b) Velocity inputs of  $R_f$  given by (36). (c) and (d) Evolutions of tracking errors  $e_m$  and  $e_n$  using the proposed IBVS controller (36).

$$v_l = 1$$
 m/s and

$$\omega_l = \begin{cases} 0.1 \text{ rad/s}, & t < 10\pi \text{ or } 10\pi + 20 \le t < 20\pi + 20 \\ 0, & \text{otherwise.} \end{cases}$$

Other conditions and all design parameters are identical with those in the first simulation. The trajectories of mobile robots are plotted in Fig. 7(a), which provides an explicit exhibition of the proposed controller's performance in an obstacle environment and how the following robot  $R_f$  moves when there are obstacles. We can see from Fig. 7(a) that the robots encounter an obstacle on the left at about 10 s. The following robot  $R_f$  controlled by the control law (36) performs a left turn to avoid the obstacle, while the robot  $R_f$  controlled by the SNGC [19] collides with the obstacle since obstacle avoidance was not considered in [19]. At about 45 s, there are two obstacles on both sides of the following robot  $R_f$ . Robot  $R_f$  under control law (36) is driven to the balanced position, that is to say, robot  $R_f$  moves along with the middle of the gap between the two obstacles in this case. The feature point tracking errors  $e_m$  and  $e_n$  of the proposed controller (36) along with their corresponding constrained boundary functions are presented in Fig. 7(c) and (d). It is clear from Fig. 7(c) and (d) that the tracking errors always stay between their corresponding boundary functions no matter how they change in the obstacle-avoidance process. After 50 s, when

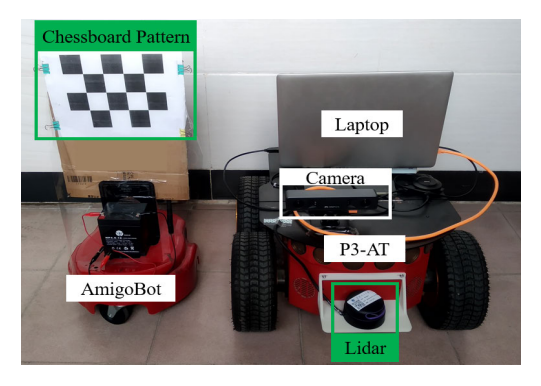


Fig. 8. Experiment setup.

there is no obstacle at the around of robot  $R_f$ ,  $e_m$  and  $e_n$  converge to small neighborhoods of zero eventually, which confirms the theoretical results presented in Theorem 1. The control inputs of the proposed controller are presented in Fig. 7(b).

# V. EXPERIMENT STUDIES

In addition to the numerical simulations, a physical experiment is also carried out to verify the efficacy of the proposed FTIBVSC. An experimental setup of two differential-driven mobile robots equipped with an onboard visual sensor and LiDAR is built, as shown in Fig. 8. The

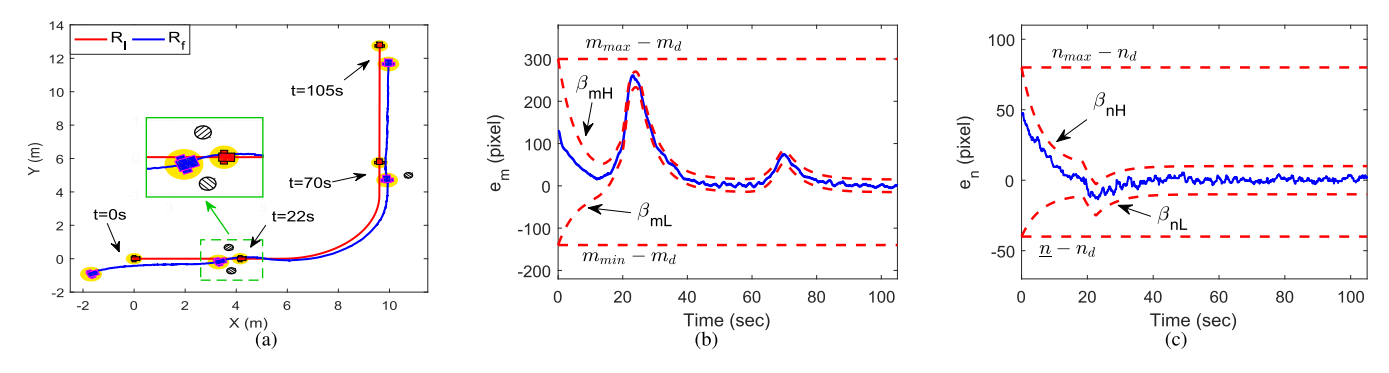


Fig. 9. Experiment results. (a) Phase-plane trajectories of the two robots. (b) and (c) Evolutions of tracking errors  $e_m$  and  $e_n$ , respectively.



Fig. 10. Snapshots taken in the experiment. (a) t = 0 s. (b) t = 22 s. (c) t = 70 s. (d) t = 105 s.

two differential-driven mobile robots are an Amigobot mobile robot and a P3-AT mobile robot from Adept MobileRobots, LLC. The Amigobot mobile serves as the moving target  $R_l$  and the P3-AT mobile robot is the follower  $R_f$ . A MYNT EYE D1000-IR-120 RGB-D camera and a SLAMTEC RPLIDAR A3 LiDAR are mounted on the following robot  $R_f$  to obtain necessary feedback information. A chessboard pattern is attached on  $R_l$ . The feature point of checkerboard pattern is extracted by the onboard RGB-D camera. The minimum distance  $d_j$ ,  $j \in \{1,2\}$ , is detected by the onboard LiDAR. The specifications of the camera are the same as that of the virtual camera mentioned in Section IV. The control algorithm is running in the laptop placed on the following robot  $R_f$  and looping at 20 Hz during the experiment.

The radii of the safe zones of  $R_l$  and  $R_f$  are  $\underline{r}_l = 0.3$ m and  $\underline{r}_f = 0.4$  m, respectively. The following robot  $R_f$  is placed 0.7 m behind the target  $R_l$ . The lower bound of n is given by  $\underline{n} = 115$ . Consequently, constraint (10) is specified by  $20 \le m \le 460$  and  $120 \le n \le 240$ . The feature height is h = 0.205 m. The desired pixel coordinate of the feature point is  $[160, 160]^T$ . The design parameters of the constrained boundary functions are set to be  $\kappa_m = \kappa_n = 0.17$ ,  $\kappa_p = 2$ ,  $k_1 = 10, k_2 = 0.25, \delta_{11} = 0.5, \delta_{21} = 2, \delta_{12} = \delta_{22} = 1, \delta_d =$ 1,  $\beta_{m,\infty} = 15$ ,  $\beta_{n,\infty} = 10$ ,  $\beta_{mL}(0) = -140$ ,  $\beta_{mH}(0) = 300$ ,  $\beta_{nL}(0) = -40$ ,  $\beta_{nH}(0) = 80$ , and  $\epsilon = 3$ . Furthermore, we select  $\underline{\beta}_{mL} = 137$ ,  $\overline{\beta}_{mL} = 267$ ,  $\underline{\beta}_{mH} = 107$ ,  $\overline{\beta}_{mH} = 297$ ,  $\underline{\beta}_{nL} = 37$ ,  $\overline{\beta}_{nL} = 57$ ,  $\underline{\beta}_{nH} = 17$ , and  $\overline{\beta}_{nH} = 77$ . Thus, we have  $-140 \le \beta_{mL}(t) < \beta_{mH}(t) \le 300$  and  $-40 \le 300$  $\beta_{mL}(t) < \beta_{mH}(t) \le 80$ . The control gains of the proposed control controller (36) are taken as  $K_1 = \text{diag}(1.2, 0.6)$  and  $K_2 = \text{diag}(0.5, 0.6)$ , and the other design parameters are  $\gamma_1 = 0.005$ ,  $\sigma_1 = 0.0015$ ,  $\gamma_2 = 0.05$ , and  $\sigma_2 = 0.005$ . The

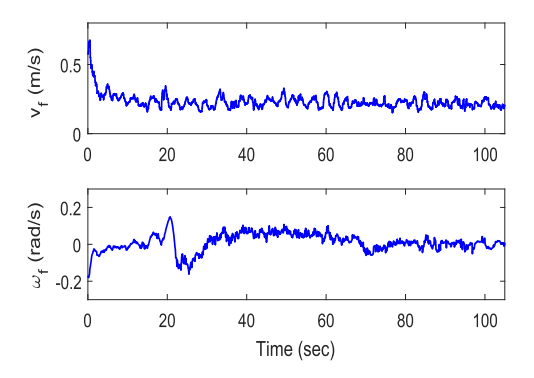


Fig. 11. Velocity inputs of  $R_f$  given by (36).

velocity inputs of the target  $R_l$  are  $v_l = 0.2$  m/s and

$$\omega_l = \begin{cases} 0.05 \text{ rad/s}, & 30 \le t < 60 \\ 0, & \text{otherwise.} \end{cases}$$

The initial poses of  $R_l$  and  $R_f$  are  $[0,0,0]^T$  and  $[-1.69,-0.92,0.42]^T$ , respectively, with  $v_f(0) = \omega_f(0) = 0$ . The experiment results are presented in Figs. 9–11. As shown in Fig. 9(a), the trajectories of  $R_l$  and  $R_f$  are depicted with their poses marked at 0, 22, 70, and 105 s, which are coincident with the snapshots in Fig. 10. Obstacle avoidance behavior and satisfactory tracking performance can be observed from Fig. 9(a). It is worth noticing that  $R_f$  performs a much smaller left turn at 70 s, compared to the one at 22 s since the obstacle on the right is further away and the overlap distance is negative. Consequently, the obstacle-avoidance behavior is suppressed and a large deviation from zero is avoided for  $e_m$ . Fig. 9(b) and (c) shows the evolutions of  $e_m$  and  $e_n$ . Though the boundary functions  $e_m$  and  $e_m$  and  $e_m$  and  $e_m$  are quite abruptly at around 20 s,  $e_m$ 

always keeps inside the feasible region that is bounded by the functions  $\beta_{mH}$  and  $\beta_{mL}$ . Moreover, both  $e_m$  and  $e_n$  converge to small neighborhoods of zero eventually. The velocity inputs  $v_f$  and  $\omega_f$  are plotted in Fig. 11. Hence, the effectiveness of the proposed control protocol in a practical scenario is verified.

#### VI. CONCLUSION

This article developed a fixed-time IBVS control design technique for moving-target tracking of nonholonomic wheeled mobile robots, where visibility maintenance, collision/obstacle avoidance, and prescribed performance were integrated in a unified BLF control design framework. The proposed control protocol only depends on the locally relative information acquired by onboard sensors, without the need of knowing the feature height and target's velocity. To cope with the issues of limited visual capability and safe navigation, FOV and time-varying boundary constraints were imposed to ensure that the following robot never breaks the visibility connection and never collides with the target and obstacles. The constrained boundary functions were proposed, which behave differently in the presence of different obstacles. When an obstacle tends to interfere between the moving target and the robot, the constrained boundary functions are deviated away from zero such that the following robot is enforced to drive away from obstacles. When there is no obstacle detected, the constrained boundaries are taken as exponentially decaying performance functions, which can describe predefined transient and steady-state performances of tracking errors. Using fixed-time stability and control Lyapunov synthesis, an FTIBVSC was designed such that tracking errors converge to a small neighborhood of the desired obstacle-avoidance trajectory in fixed time while guaranteeing visibility maintenance and obstacle/collision avoidance. Simulation and experiment results showed the effectiveness of the proposed fixed-time IBVS control protocol.

# REFERENCES

- [1] S. Hutchinson, G. D. Hager, and P. I. Corke, "A tutorial on visual servo control," *IEEE Trans. Robot. Autom.*, vol. 12, no. 5, pp. 651–670, Oct. 1996.
- [2] B. Li, X. Zhang, Y. Fang, and W. Shi, "Visual servoing of wheeled mobile robots without desired images," *IEEE Trans. Cybern.*, vol. 49, no. 8, pp. 2835–2844, Aug. 2019.
- [3] X. Zhang, R. Wang, Y. Fang, B. Li, and B. Ma, "Acceleration-level pseudo-dynamic visual servoing of mobile robots with backstepping and dynamic surface control," *IEEE Trans. Syst., Man, Cybern., Syst.*, vol. 49, no. 10, pp. 2071–2081, Oct. 2019.
- [4] H. Shi, G. Sun, Y. Wang, and K.-S. Hwang, "Adaptive image-based visual servoing with temporary loss of the visual signal," *IEEE Trans. Ind. Informat.*, vol. 15, no. 4, pp. 1956–1965, Apr. 2019.
- [5] X. Liang, H. Wang, W. Chen, D. Guo, and T. Liu, "Adaptive image-based trajectory tracking control of wheeled mobile robots with an uncalibrated fixed camera," *IEEE Trans. Control Syst. Technol.*, vol. 23, no. 6, pp. 2266–2282, Nov. 2015.
- [6] C. P. Bechlioulis, S. Heshmati-alamdari, G. C. Karras, and K. J. Kyriakopoulos, "Robust image-based visual servoing with prescribed performance under field of view constraints," *IEEE Trans. Robot.*, vol. 35, no. 4, pp. 1063–1070, Aug. 2019.
- [7] B. Li, X. Zhang, Y. Fang, and W. Shi, "Visual servo regulation of wheeled mobile robots with simultaneous depth identification," *IEEE Trans. Ind. Electron.*, vol. 65, no. 1, pp. 460–469, Jan. 2018.
- [8] X. Zhang, Y. Fang, and N. Sun, "Visual servoing of mobile robots for posture stabilization: From theory to experiments," *Int. J. Robust Nonlinear Control*, vol. 25, no. 1, pp. 1–15, Jan. 2015.

- [9] B. Penin, P. R. Giordano, and F. Chaumette, "Vision-based reactive planning for aggressive target tracking while avoiding collisions and occlusions," *IEEE Robot. Autom. Lett.*, vol. 3, no. 4, pp. 3725–3732, Oct. 2018.
- [10] D. J. Agravante, G. Claudio, F. Spindler, and F. Chaumette, "Visual servoing in an optimization framework for the whole-body control of humanoid robots," *IEEE Robot. Autom. Lett.*, vol. 2, no. 2, pp. 608–615, Apr. 2017.
- [11] G. López-Nicolás, M. Aranda, and Y. Mezouar, "Adaptive multirobot formation planning to enclose and track a target with motion and visibility constraints," *IEEE Trans. Robot.*, vol. 36, no. 1, pp. 142–156, Feb. 2020
- [12] S.-L. Dai, K. Lu, and J. Fu, "Adaptive finite-time tracking control of nonholonomic multirobot formation systems with limited field-ofview sensors," *IEEE Trans. Cybern.*, vol. 52, no. 10, pp. 10695–10708, Oct. 2022.
- [13] S. S. Ge, X. Liu, C.-H. Goh, and L. Xu, "Formation tracking control of multiagents in constrained space," *IEEE Trans. Control Syst. Technol.*, vol. 24, no. 3, pp. 992–1003, May 2016.
- [14] T. P. Nascimento, A. G. S. Conceição, and A. P. Moreira, "Multi-robot nonlinear model predictive formation control: The obstacle avoidance problem," *Robotica*, vol. 34, no. 3, pp. 549–567, Mar. 2016.
- [15] H. Rezaee and F. Abdollahi, "A decentralized cooperative control scheme with obstacle avoidance for a team of mobile robots," *IEEE Trans. Ind. Electron.*, vol. 61, no. 1, pp. 347–354, Jan. 2014.
- [16] X. Jin, S.-L. Dai, J. Liang, and D. Guo, "Multirobot system formation control with multiple performance and feasibility constraints," *IEEE Trans. Control Syst. Technol.*, vol. 30, no. 4, pp. 1766–1773, Jul. 2022.
- [17] K. Lu, S.-L. Dai, and X. Jin, "Cooperative constrained enclosing control of multirobot systems in obstacle environments," *IEEE Trans. Control Netw. Syst.*, early access, Jul. 26, 2023, doi: 10.1109/TCNS.2023.3299151.
- [18] J. Lin, Z. Miao, H. Zhong, W. Peng, Y. Wang, and R. Fierro, "Adaptive image-based leader-follower formation control of mobile robots with visibility constraints," *IEEE Trans. Ind. Electron.*, vol. 68, no. 7, pp. 6010–6019, Jul. 2021.
- [19] Z. Miao, H. Zhong, J. Lin, Y. Wang, Y. Chen, and R. Fierro, "Vision-based formation control of mobile robots with FOV constraints and unknown feature depth," *IEEE Trans. Control Syst. Technol.*, vol. 29, no. 5, pp. 2231–2238, Sep. 2021.
- [20] I. M. Delimpaltadakis, C. P. Bechlioulis, and K. J. Kyriakopoulos, "Decentralized platooning with obstacle avoidance for car-like vehicles with limited sensing," *IEEE Robot. Autom. Lett.*, vol. 3, no. 2, pp. 835–840, Apr. 2018.
- [21] C. P. Bechlioulis and G. A. Rovithakis, "Robust adaptive control of feedback linearizable MIMO nonlinear systems with prescribed performance," *IEEE Trans. Autom. Control*, vol. 53, no. 9, pp. 2090–2099, Oct. 2008.
- [22] B. Ning, Q.-L. Han, and Z. Zuo, "Practical fixed-time consensus for integrator-type multi-agent systems: A time base generator approach," *Automatica*, vol. 105, pp. 406–414, Jul. 2019.
- [23] X. Jin, "Adaptive fixed-time control for MIMO nonlinear systems with asymmetric output constraints using universal barrier functions," *IEEE Trans. Autom. Control*, vol. 64, no. 7, pp. 3046–3053, Jul. 2019.
- [24] S.-L. Dai, S. He, Y. Ma, and C. Yuan, "Distributed cooperative learning control of uncertain multiagent systems with prescribed performance and preserved connectivity," *IEEE Trans. Neural Netw. Learn. Syst.*, vol. 32, no. 7, pp. 3217–3229, Jul. 2021.
- [25] Y. Xu, S. Zhao, D. Luo, and Y. You, "Affine formation maneuver control of high-order multi-agent systems over directed networks," *Automatica*, vol. 118, Aug. 2020, Art. no. 109004.
- [26] H.-Q. Wang, B. Chen, and C. Lin, "Adaptive neural tracking control for a class of stochastic nonlinear systems," *Int. J. Robust Nonlinear Control*, vol. 24, no. 7, pp. 1262–1280, May 2014.
- [27] S.-L. Dai, K. Lu, and X. Jin, "Fixed-time formation control of unicycletype mobile robots with visibility and performance constraints," *IEEE Trans. Ind. Electron.*, vol. 68, no. 12, pp. 12615–12625, Dec. 2021.
- [28] Z. Zuo, "Nonsingular fixed-time consensus tracking for second-order multi-agent networks," *Automatica*, vol. 54, pp. 305–309, Apr. 2015.
- [29] Z. Zuo, B. Tian, M. Defoort, and Z. Ding, "Fixed-time consensus tracking for multiagent systems with high-order integrator dynamics," *IEEE Trans. Autom. Control*, vol. 63, no. 2, pp. 563–570, Feb. 2018.
- [30] Z. Cai, M. S. deQueiroz, and D. M. Dawson, "A sufficiently smooth projection operator," *IEEE Trans. Autom. Control*, vol. 51, no. 1, pp. 135–139, Jan. 2006.

[31] E. Malis and F. Chaumette, "2 1/2 D visual servoing with respect to unknown objects through a new estimation scheme of camera displacement," *Int. J. Comput. Vis.*, vol. 37, pp. 79–97, Jun. 2000.



Shi-Lu Dai (Member, IEEE) received the B.Eng. degree in thermal engineering and the M.Eng. and Ph.D. degrees in control science and engineering from Northeastern University, Shenyang, China, in 2002, 2006, and 2010, respectively.

He was a Visiting Student with the Department of Electrical and Computer Engineering, National University of Singapore, Singapore, from November 2007 to November 2009, and a Visiting Scholar at the Department of Electrical Engineering, University of Notre Dame, Notre Dame, IN, USA, from

October 2015 to October 2016. Since 2010, he has been with the School of Automation Science and Engineering, South China University of Technology, Guangzhou, China, where he is currently a Professor. His current research interests include adaptive and learning control, and distributed cooperative systems.



**Jianjun Liang** received the B.E. and M.Eng. degrees in automatic control from the South China University of Technology, Guangzhou, China, in 2019 and 2022, respectively.

He is currently an Algorithm Design Engineer with Shenzhen Dajiang Innovation Technology Company Ltd., Shenzhen, China. His research interests include dynamic path planning and vision-based control systems.



**Ke Lu** received the B.E. degree in material engineering from Nanjing Forestry University, Nanjing, China, in 2015, and the M.Sc. degree in mechanical and automation engineering from The Chinese University of Hong Kong, Hong Kong, in 2017. He is currently pursuing the Ph.D. degree in control science and engineering with the School of Automation Science and Engineering, South China University of Technology, Guangzhou, China.

His current research interests include adaptive control systems, and coordination and control of multiagent systems.



**Xu Jin** (Member, IEEE) received the B.Eng. degree (Hons.) in electrical and computer engineering from the National University of Singapore, Singapore, in 2013, the Master of Applied Science (M.A.Sc.) degree in electrical and computer engineering from the University of Toronto, Toronto, ON, Canada, in 2015, and the Master of Science (M.S.) degree in mathematics and the Doctor of Philosophy (Ph.D.) degree in aerospace engineering from the Georgia Institute of Technology, Atlanta, GA, USA, in 2018 and 2019, respectively.

He is currently an Assistant Professor with the Department of Mechanical and Aerospace Engineering, University of Kentucky, Lexington, KY, USA. He has authored/coauthored over 50 peer-reviewed journal articles and conference papers. His current research interests include adaptive and iterative learning control, fault-tolerant control, and nonlinear systems control, with applications to intelligent vehicles, autonomous robots, and multiagent systems

Dr. Jin has been a reviewer for over 20 journals in the areas of control systems and applications.